Novel design of a high efficiency multi-bed active magnetic regenerator heat pump

Dall'Olio, S.; Masche, M.; Liang, J.; Insinga, A.R.; Eriksen, D.; Bjørk, R.; Nielsen, K.K.; Barcza, A.; Vieyra, H.A.; Beek, Niels v.

Total number of authors:
13

Published in:
International Journal of Refrigeration

Link to article, DOI:
10.1016/j.ijrefrig.2021.09.007

Publication date:
2021

Document Version
Publisher's PDF, also known as Version of record

International Journal of Refrigeration 132 (2021) 243–254

Contents lists available at ScienceDirect

International Journal of Refrigeration

journal homepage: www.elsevier.com/locate/ijrefrig

Novel design of a high efficiency multi-bed active magnetic regenerator heat pump

Nouvelle conception d'une pompe à chaleur à régénérateur magnétique actif à lits multiples et à haut rendement

S. Dall'Olio [a,b], M. Masche [a], J. Liang [a], A.R. Insinga [a], D. Eriksen [1,a], R. Bjørk [a], K.K. Nielsen [a,2], A. Barcza [c], H.A. Vieyra [c], Niels V. Beek [d], H. Neves Bez [a,e,3], K. Engelbrecht [a], C.R.H. Bahl [a,*]

[a] Department of Energy Conversion and Storage, Technical University of Denmark - DTU, Anker Engelunds Vej B301, 2800 Kgs. Lyngby, Denmark
[b] Faculty of Mechanical Engineering, Laboratory for Refrigeration and District Energy, LAHDE University of Ljubljana, Aškerceva 6, SI-1000 Ljubljana, Slovenia
[c] Vacuumschmelze GmbH & Co. KG, Grüner Weg 37, 63450 Hanau, Germany
[d] Bakker Magnetics BV, Science Park Eindhoven 5502, 5692 ELSon, The Netherlands
[e] POLO - Research Laboratories for Emerging Technologies in Cooling and Thermophysics, Department of Mechanical Engineering, Federal University of Santa Catarina (UFSC), Florianópolis, SC, 88040-900, Brazil

ARTICLE INFO

Keywords:
Magnetic refrigeration
Magnetocaloric effect
Heat pump
Active magnetic regenerator
Mots clés:
Froid magnétique
Effet magnétocalorique
Pompe à chaleur
Régénérateur magnétique actif

ABSTRACT

The design of a rotary active magnetic regenerator heat pump device with a multi-bed concept is presented. Important design features are the rotating two-pole magnet assembly, the laminated iron ring, the 13 fixed tapered regenerator beds, and the dynamically adjustable parallel flow circuit. The optimized magnet design was developed with optimally shaped segments and optimum remanence for the desired magnetic field distribution oscillating between 0 and 1.44 T in the air gap. The iron ring was laminated to reduce the eddy currents, allowing the device to run at cycle frequencies up to 3 Hz. The design of the regenerator housing was optimized with respect to parasitic losses and even flow distribution in both directions. Employing 3.4 kg of $La(Fe,Mn,Si)_{13}H_y$ (CALORIVAC HS) refrigerant and at a hot reservoir temperature of 295 K and a cycle frequency of 0.5 Hz, the heat pump achieved a maximum second-law efficiency of 20.6 %, while providing a heating load of 340 W with a heating COP of 6.7 at a 10.3 K span. The COP values presented only consider the magnetic power and ideal pump power delivered to the AMR, neglecting the pump efficiency. At 1.2 Hz, the device produced a maximum heating power of 950 W while maintaining a 5.6 K span, resulting in a heating coefficient of performance and second-law efficiency of 7.0 and 11.6 %, respectively. The performance demonstrated in this paper could be an important milestone in the development of future magnetocaloric devices.

1. Introduction

Over the past century, the world energy consumption from buildings has grown rapidly, particularly due to population growth, more time spent indoors, and increased demand for building functions. In Europe, for instance, cooling and heating energy consumption in buildings account for approx. 40% of the total energy demand. Therefore, improving the building energy efficiency is one of the key priorities to achieve the ambitious goals of limiting global temperature rise to 1.5°C and supporting a transition to climate neutrality by 2050, envisaged by the European Green Deal (European Commission, 2019). European countries must set cost-efficient and optimal energy efficiency requirements for new buildings and for the retrofit of existing building elements like air conditioners,

* Corresponding author at: Department of Energy Conversion and Storage, Technical University of Denmark - DTU, Anker Engelunds Vej B301, 2800 Kgs. Lyngby, Denmark
E-mail address: chrb@dtu.dk (C.R.H. Bahl).
[1] Presently at Weibel Scientific A/S, Solvang 30, 3450 Lillerød, Denmark
[2] Presently at BEC Financial Technologies, Havsteensvej 4, 4000 Roskilde, Denmark
[3] Deceased, January 2021.

https://doi.org/10.1016/j.ijrefrig.2021.09.007
Received 3 May 2021; Received in revised form 2 September 2021; Accepted 6 September 2021
Available online 11 September 2021

Nomenclature

Acronyms

AMR	Active magnetic regenerator
CAD	Computer-aided design
COP	Coefficient of performance
DTU	Technical University of Denmark
FOPT	First-order phase transition
MCE	Magnetocaloric effect
MCM	Magnetocaloric material
NTU	Number of transfer unit
SLS	Selective Laser Sintering

Symbols

B	Magnetic flux density [T]
B_r	Remanence [T]
c_f	Specific heat of the fluid [J kg^{-1} K^{-1}]
dV	Magnet integration volume [m^3]
E_{mag}	Magnetic energy [J]
f	Operating frequency [Hz]
H	Magnetic field intensity [A m^{-1}]
L	Length of MCM layer [m]
p	Pressure [bar]
$\dot{Q}_c$	Cooling power [W]
$\dot{Q}_h$	Heating power [W]
T_{cold}	Cold reservoir temperature [K]
T_{Curie}	Curie temperature [K]
T_{hot}	Hot reservoir temperature [K]
$\dot{V}$	Volumetric fluid flow rate [L h^{-1}]
$\dot{W}_{losses}$	Mechanical losses in the drive system [W]
$\dot{W}_{mag}$	Magnetic power into the regenerator [W]
$\dot{W}_{pump}$	Pumping power [W]
$\dot{W}_{shaft}$	Shaft power [W]
ΔT	Curie temperature spacing [K]
ΔT_{span}	Temperature span, T_{hot}-T_{cold} [K]
η_{II}	Second-law efficiency [%]
Λ_{cool}	Magnet characterization parameter [T$^{2/3}$]
ρ_f	Density of the working fluid [kg m^{-3}]
Γ	Shaft torque [N m]

refrigerators, and heat pumps.

Heat pumps represent a promising technology that can contribute to the European climate targets toward a carbon-neutral Europe. Due to their versatility, they can provide renewable cooling, space heating, and hot water. As most of this demand is traditionally met by fossil fuels, the share of renewables in the cooling and heating sector can be significantly increased. Conventional heat pumps are based on the vapor-compression refrigeration cycle in which thermal energy is transferred from a low-temperature heat source to a building's high-temperature sink using a thermodynamic cycle based on compression and expansion of a refrigerant. These refrigerants can be hazardous (e.g., NH_3), greenhouse gases (e.g., HFCs), or flammable (e.g., HCs) (Dincer and Kanoğlu, 2003). It is hence obvious to think about alternative cooling/heating technologies using environmentally friendly refrigerants, such as magnetocaloric heat pumps.

Magnetocaloric heat pumps are built on the active magnetic regenerator (AMR) system that exploits the magnetocaloric effect (MCE) of a solid-state, ferromagnetic refrigerant. The MCE causes the refrigerant to increase in temperature when magnetized and cool when demagnetized. The temperature change in the refrigerant is used to build a magnetic cooling/heating cycle, comprising (i) magnetization, (ii) flow and heat rejection to ambient (cold-to-hot blow), (iii) demagnetization, and (iv) flow and heat absorption (hot-to-cold blow). In the thermodynamic cycle, solid-state refrigerants with properties coupled to temperature and magnetic field are used. Since magnetocaloric materials (MCMs) are solid at room temperature, they have no direct global warming potential (Kitanovski et al., 2015). In particular, MCMs with a first-order phase transition (FOPT) that experience a discontinuous, magneto-structural phase change associated with a strong caloric effect are very promising for magnetocaloric heat pumps (Lei et al., 2016a). Due to the reversible nature of the MCE, AMR devices have the potential for a high coefficient of performance (COP) and hence become a more efficient alternative to conventional vapor-compression systems (Bansal et al., 2012; Qian et al., 2016).

Using the MCM to cool a reservoir was first demonstrated nearly 100 years ago, but the technology did not become generally considered as a viable alternative to vapor compression until the regenerative cycles with water-based heat transfer fluids were demonstrated, see, e.g., Barclay, (1990). Since the 1980s, AMR devices based on various magnetic field sources and mechanical implementations have been reported (Kitanovski et al., 2015). Based on results from these demonstrators, AMR devices based on a continuously rotating regenerator using a water-based heat transfer fluid and a permanent magnet system were developed. In these systems, the regenerator rotates relative to the permanent magnet, where either the magnet or the regenerator can rotate, and a pump continuously pumps heat transfer fluid through an array of small regenerator beds. These rotary AMR beds constantly use the magnetic field volume and absorb a constant heat load at the cold reservoir. Thus they are more compact and cost-effective than other AMR configurations.

1.1. State-of-the-art AMR prototypes

In the last decade, several rotary AMR devices have been reported that can operate at or near commercially relevant cooling loads and temperature spans (Kitanovski et al., 2015) . Many research groups use gadolinium (Gd) as a benchmark refrigerant material in their AMR devices, because it is a pure metal with well-known, attractive magnetocaloric properties. In 2010, an AMR design was presented consisting of a fixed permanent magnet assembly with a peak flux density (B_{max}) of 0.98 T, a rotating drum with chambers for 34 AMRs filled with a total of 0.6 kg of Gd plates (0.3 mm in thickness), and distilled water as the heat transfer fluid (Tušek et al., 2010). The primary goal of the device was to build a small and compact AMR prototype with components of high quality that can be machined using standard tools and at a low cost. However, the authors did not report any performance data.

In 2010, Tura and Rowe (2010) developed an AMR system featuring two cylindrical nested Halbach arrays with a maximum field of 1.47 T and two stationary AMRs connected by a fluid displacer to distribute the water-glycol (80:20) mix in an oscillating flow. At an operating frequency of 4 Hz, the device using 0.11 kg of Gd spheres produced a maximum no-load temperature span of 29 K and a maximum cooling load of 50 W over a 10 K temperature span with a COP of 0.3-0.5. The maximum COP of 1.6 was achieved when the AMR device provided a cooling load of 50 W over a 2.5 K span and at 1.4 Hz. Later, this AMR design was modified by employing three nested Halbach arrays in a counter-rotating configuration with a peak field strength of B_{max}=1.54 T (Arnold et al., 2014). With the improved design of the permanent magnet and operating with 0.65 kg of Gd spheres, the authors reported a maximum no-load temperature span of 33 K and a maximum zero-span cooling power of 96 W at 0.8 Hz. No values for the COP or second-law efficiency have been reported, as the power consumption was not measured. Okamura and Hirano (2013) presented a 1.1 T magnetic refrigerator employing 1 kg Gd that provided a maximum cooling power of about 200 W and a maximum COP of 2.5 for a 5 K span.

The magnetocaloric group at the Technical University of Denmark

(DTU) has previously reported two rotary AMR systems. In 2013, a device with a four-pole permanent magnet assembly with $B_{max} = 1.24$ T and 24 regenerator beds filled with a total of 2.8 kg of Gd spheres (0.25-0.8 mm) demonstrated a maximum no-load temperature span of 25.4 K at 2 Hz and a maximum zero-span cooling power of 1010 W at 1.8 Hz (Bahl et al., 2013). The maximum COP measured was 1.62 when absorbing 400 W cooling power over a 1.5 K span and at 1.5 Hz, while a peak second-law efficiency of 5.6 % was obtained at a 12.9 K span for the same thermal load, which corresponds to a COP of 1.23 (Lozano et al., 2013). The second AMR system was a compact system with a two-pole permanent magnet with $B_{max} = 1.13$ T (Eriksen et al., 2015). The system was designed with 11 regenerator beds, each filled with spheres of Gd and different compositions of $Gd_{100-x}Y_x$, to improve magnetic force balance and a combination of poppet valves on the hot side of the regenerator and check valves on the cold side of the regenerator to direct fluid flow with low parasitic losses. At a frequency of 0.75 Hz, the AMR demonstrated a maximum no-load temperature span of 20 K and a maximum cooling power of ca. 140 W over a span of around 6 K, which corresponds to a COP of 4.6. In 2016, the system reported the highest second-law efficiency of a rotary magnetocaloric AMR device, which was 18 % at a cooling load of 81.5 W and COP of 3.6 for a span of 15.5 K (Eriksen et al., 2016).

In 2014, Aprea et al. (2014) constructed a refrigerator with a rotating two-pole magnet (B_{max}=1.25 T) and eight fixed AMR beds. Each bed contained 0.15 kg Gd spheres (0.4-0.5 mm). At 0.93 Hz, the device provided a maximum no-load span of 11.9 K and a maximum zero-span cooling power of 200 W. A maximum value of 2.5 for the COP was achieved for a 200 W cooling power at a 0 K span and at 0.38 Hz (Aprea et al., 2016). Cheng et al. (2016) built an AMR with two concentric Halbach arrays (B_{max}=1.5 T) rotating over a multi-layer bed filled with 1.5 kg Gd and GdEr particles. At 2 Hz, the AMR produced a maximum no-load span of above 25 K and a maximum cooling power of 147 W. Trevizoli et al. (2015) designed an AMR with a nested Halbach cylinder array with a peak magnetic field of 1.69 T. Employing ca. 200 g of Gd spheres (0.5-0.6mm) in a single regenerator, the device achieved a maximum temperature span of 28 K at 0.5 Hz for a cooling load of 3.6 W and a maximum zero-span cooling power of about 54 W at 1 Hz. At 0.25 Hz, the highest COP value of 4.6 was reported when the AMR produced a cooling power of 11 W at a 5 K span, while a peak second-law efficiency of 13.5 % was obtained for a cooling power of 6.5 W over a 15 K span.

Recently, rotary AMR devices have been reported that employ multi-bed regenerators filled with FOPT alloys, such as LaFeSi (Lionte et al., 2018), LaFeSiH (Jacobs et al., 2013), LaFeMnSiH (Dall'Olio et al., 2017a; Monfared and Palm, 2016) or manganese-based compounds (Sota et al., 2016). These alloys have the potential to replace Gd, as they exhibit a larger isothermal entropy change and hence a larger MCE, which is needed to achieve higher cooling capacities (Lei et al., 2016b), especially when the temperature span is below 30 K (Lei et al., 2016a). The potential of FOPT-based AMRs was demonstrated by Jacobs et al. (2013), who built a large-scale AMR device with a rotating Halbach array (B_{max}=1.44 T) and twelve fixed AMR beds. Each bed contained six layers of LaFeSiH spheres (0.18-0.25 mm) of different Curie temperatures (T_{Curie}). At 4 Hz, the device using 1.52 kg of refrigerant produced a peak zero-span cooling power of 3042 W with a COP of 2.5 and a maximum no-load temperature span of 18 K. At an 11.0 K span, a promising cooling power of 2502 W with an electrical COP of 1.9 was obtained. A comprehensive list of rotary AMR devices presented before 2019 is described in review articles (Greco et al., 2019; Gschneidner Jr. and Pecharsky, 2008; Yu et al., 2010), reporting around 80 AMR prototypes.

1.2. Design philosophy

There is no unique way to build a high-performance AMR device. A number of parameters constrain the design of an AMR system. Among these are the type of magnetocaloric material (morphology, mass), the type of fluid flow and flow controllers, the type of relative motion between magnet and regenerators, the regenerator geometry, and the type of magnet (material, mass, number of poles). It is hence important to find a good balance between regenerator geometry, operating frequency, magnetic forces, and practical details such as sealing (Rowe and Barclay, 2003). Especially, the latter one can negate any useful heating power. With these in mind, the magnetocaloric group at DTU designed a new magnetocaloric heat pump prototype, called MagQueen, which was designed to supply the heating needs of a typical Danish single-family house. According to the trends in the scientific field, a temperature span of 25-30 K with a permanent magnet is highly competitive, and a high frequency operation is no longer mandatory. Instead, there is an increased focus on device efficiency and high temperature span. The MagQueen prototype, which was inspired by other high-performance AMR designs reported in the literature (Aprea et al., 2014; Eriksen et al., 2015; Jacobs et al., 2013), provides a path towards higher efficiency with the following design goals:

- Increase the fluid flow rate while maintaining a high number of transfer units (NTU) in the regenerator
- Reduce the eddy current heating generated by the magnet
- Achieve an accurate flow system
- Increase the temperature span of the AMR
- Increase the internal magnetic field of the regenerator

This paper describes the design of the MagQueen prototype in detail and the updates made to improve its performance and prepare it for implementation in the innovative multi-source heat pump concept within the RES4BUILD project. In this concept, the MagQueen heat pump will be coupled to a vapor-compression heat pump in a cascade configuration. The source of the MagQueen heat pump will be a borehole thermal energy storage. MagQueen in turn provides heat to the evaporator of a vapor compression heat pump that can provide heating and hot water temperatures. As an alternative heat source, low-temperature heat can also be supplied by solar thermal collectors through solar buffer tanks to the MagQueen heat pump ("RES4BUILD," 2021). To the best of our knowledge, a magnetocaloric heat pump for commercial applications has not yet been demonstrated. Hence, the development of new prototypes with a cooling/heating load suitable for commercialization and with efficiencies higher than those found in conventional vapor compression systems is an important activity.

2. Design concept

A picture of MagQueen and its main design components is shown in Figure 1 and Video 1. It mainly consists of a 13-side polygon made from soft magnetic steel (S235JR). As this is magnetically similar to being

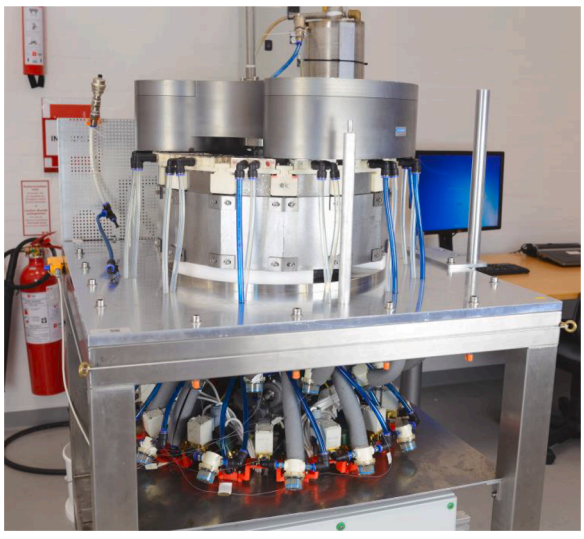

Fig. 1. Picture of the MagQueen prototype, showing the components discussed in the text.

pure iron, we will refer to the steel as iron in the following. The polygon has 13 protruding teeth on top of which the 13 AMR beds are mounted. An iron yoke containing the two-pole permanent magnet assembly is mounted on a shaft above the iron ring, and the magnet assembly is rotated by an electric motor. All permanent magnet material is mounted within the yoke. A torque meter is installed on the shaft to measure the instantaneous electrical power needed to rotate the magnet. To control the flow for each AMR, two solenoid valves and two check valves are used (Figure 2). This combination ensures that flow to each regenerator can be controlled individually, the fluid flow rate can change quickly, and fluid flow will be unidirectional. The fluid is circulated by a centrifugal pump and passes through the different components of the hydraulic system, such as regenerators and external heat exchangers (heat sink and heat source). In parallel to the main flow circuit, a bypass loop is installed to allow a finer regulation of the flow rate through the device. The fluid system is installed under the top aluminum plate. The whole MagQueen device weighs approximately 750 kg, primarily due to the iron volume in the ring and the yoke. To give more details about the prototype, all the main components and their characteristics are listed in Table 1. The total system is shown in Figure 1, and a cross-section of the system is given in Figure 2. The design of each subsystem is described in the following sections.

2.1. Permanent magnet assembly

To design the magnet of MagQueen, the main recommendations presented in (Bjørk et al., 2010) to maximize the global magnet design efficiency, have been followed. In particular, the most relevant criteria suggest that the magnet should be utilized at all times and that the flux density in the low flux density region must be as low as possible. Finally, flux guides of soft magnetic material should be used to minimize magnetic flux leakage to the surroundings.

With these ideas in mind, the permanent magnet assembly for the heat pump has been designed through a novel 'virtual magnet' approach, as described in (Insinga et al., 2019,2016). This approach is an optimization method and is based on the reciprocity theorem, an energy equivalence principle of magnetostatics, which can be expressed by the following equation:

$$\int dV\ B_{r1}(x)\cdot H_2(x) = \int dV\ B_{r2}(x)\cdot H_1(x) \tag{1}$$

Where $B_{r1}(x)$ is the remanence of the virtual system 1 at the point x, H_1 is the magnetic field generated by B_{r1}, and similarly for the virtual system 2. In this equation, the virtual remanence B_{r2} is interpreted as an objective vector field.

As the magnetic field source is the single most expensive part of an AMR device (Bjørk et al., 2016; Teyber et al., 2017), ideally, the required field should be produced using the minimum possible volume of

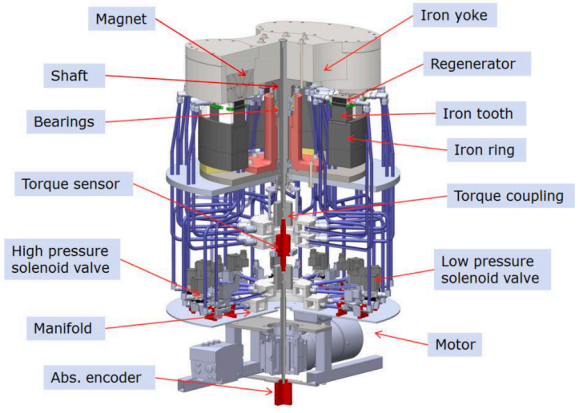

Fig. 2. 3D cross section view of MagQueen showing all its main components.

Table 1
Technical properties of the AMR.

Component	Model	Manufacturer
Regenerator beds	13 tapered (10°) with nylon housing with a stainless steel lid	3D printed
MCM material	10 layers of $La(Fe,Mn,Si)_{13}H_y$ (CALORIVAC HS), 3.41 kg in total	Vacuumschmelze
Magnet	Two-pole NdFeB magnet from N50 and N50M	Bakker Magnetics
Encoder	HS10	Hohner Automation
Motor	SK92172.1A-80SH/4 TF IG22 TI4	Nord
Motor Frequency inverter	SK 200E-550-123-A	DRIVESYSTEMS
NI chassis	cRIO-9066	National
NI cards	NI 9203, NI 9217, NI 9472, NI 9213	Instruments
Torque transducer	Model 8645-5175	Burster
Hot inlet solenoid valves	SCE 238	ASCO
Hot outlet solenoid valves	33VX232FGAXB	SMC
Pump	CRNE 1-9	Grundfos
Flow meter	FPR 200	OMEGA
Thermocouples	E-type thermocouples coupled to NI-9213 data acquisition card	OMEGA
Thermistors	TRC#P1A2X	Newtronic
Heating unit	Fluid circulation heater DN 50	Vulcanic
Electrical power meter	G2BA400V12A 4...20mA	Tele Hasse
Pressure transmitter	P20-408-1110	Nöding Meßtechnik

permanent magnets. In order to accomplish this goal, the magnetic circuit should be designed in such a way that the only air gap is the region occupied by the AMR, so that the total magnetic reluctance of the circuit is minimal. For this reason, our design is composed of two parts: the bottom iron part and the top part, which includes the permanent magnets encased in an iron yoke. The magnetic circuit is shown in Figure 3, where the direction of the magnetic flux is schematically illustrated by the red arrows. The purpose of the iron protrusions ("teeth") above the bottom iron ring is to concentrate the magnetic flux inside the 13 regenerator beds. We decided to use an odd number of AMR beds with a two-pole magnet in order to limit the amplitude of the cogging torque, which would otherwise harm the performance of the device.

In fact, in addition to employing the virtual magnet method to design the permanent magnet segments, all the parameters determining the geometry of the magnetic circuit have been optimized using parametric optimization to maximize the performance while limiting the amount of permanent magnet material and satisfying the various constraints. While the virtual magnet method assumes a linear objective, i.e., the z component of the flux density averaged over the high-field region, for optimizing the various geometrical parameters, the figure of merit Λ_{cool} was employed. Λ_{cool} is a well-established parameter for optimizing magnet designs of magnetic refrigerators, and it favors designs that produce a high magnetic flux density in a large volume using a minimum of magnetocaloric material (Bjørk et al., 2010).

Figure 3 shows the final design of the magnet, which is composed of two geometrically identical halves with the magnetic field oriented in opposite directions. The two halves are epoxy-glued into the iron yoke, which covers all the surfaces of the magnet, except the ones facing the air gap. This design strategy focuses the field in the high-field region of the air gap while minimizing the magnetic flux leakage. Each half is made up of 28 segments, which are glued together. In total, there are only six different shapes of the segments. The magnet segments are all sintered NdFeB. The middle group of segments (central in the half) are grade N50 (remanence: 1.44 T and coercivity: 860 kA m^{-1}), while the outer segments are grade N50M (remanence: 1.44 T and coercivity: 980 kA m^{-1}). The reason for utilizing different grades of NdFeB for the

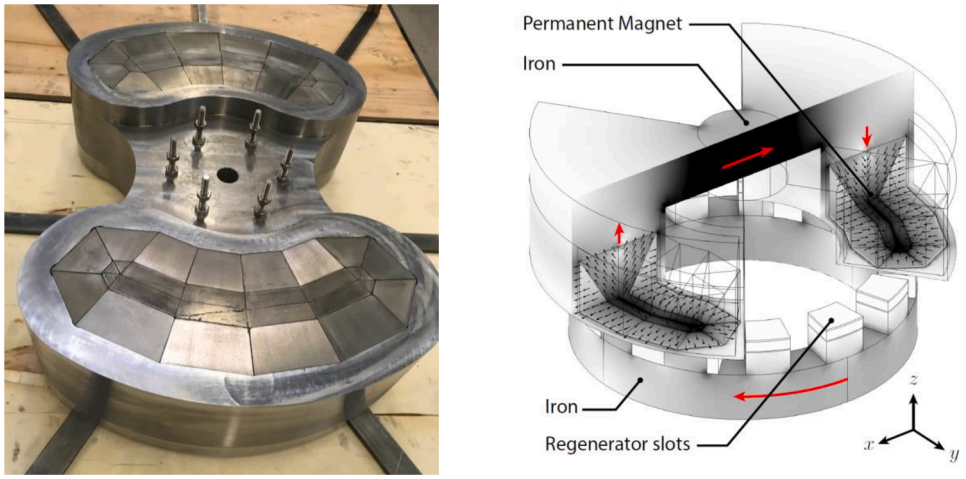

Fig. 3. (a) The two halves of the magnet seen from below. (b) The geometry of the magnet segmentation.

different parts is that the outer segments experience an opposing field that is stronger than the coercivity of N50, and would thus undergo nonlinear demagnetization if that material was used. It was then decided to utilize N50M to avoid this detrimental effect. On the other hand, for the segments located in the central region, the less expensive grade N50 is appropriate since the opposing field is less intense in that area. The total volume of permanent magnet material is 10531.8 cm^3, while the volume of the high flux density region is 1667.4 cm^3.

Figure 4 shows the z component of the magnetic flux density experienced by a single AMR at four positions above a bed, as indicated in the inset. The magnetic field was measured by a Hall sensor at room temperature (about 296 K) and at a 0 K temperature span in the regenerators. The curves illustrate the magnetic flux density profile for a 360° rotation of the magnet starting at the ramp between the zero-field and high field regions. The black line represents the averaged magnetic field over the four positions depicted on the lid of the AMR, and the dashed blue line shows the results obtained from a numerical model of the assembly made in COMSOL Multiphysics. It is shown that the zero-field and high-field region span a wide angle, and that the magnetic field ramps relatively quickly from the zero-field region to the high-field region and vice versa. The flux density in the high-field region is fairly constant, and is very low in the zero-field region, as desired. However, there is some variation along the radial direction. The maximum mean magnitude of the flux density reaches about 1.6 T in the high-field region. However, the flux density will be a little lower within the actual regenerator volume, as it is further from the magnet poles than the lid. A volume average value of $B_{avg} = 1.44$ T has been calculated within the regenerator volume by the COMSOL numerical model.

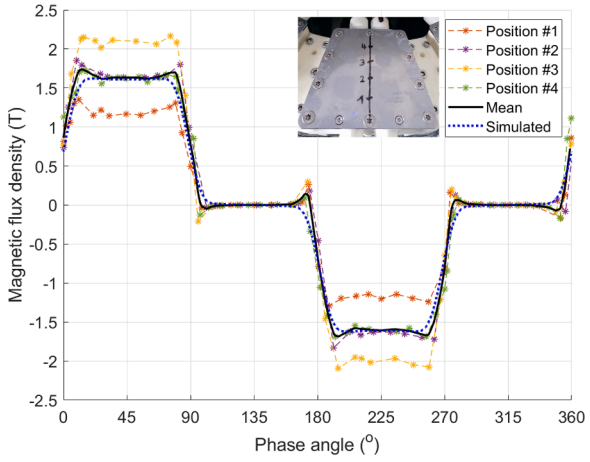

Fig. 4. Experimental magnetic flux density profile measured by a Hall probe at four positions on top of the regenerator lid and the simulated flux density found from a COMSOL model.

2.2. Laminated iron ring

In MagQueen, the large permanent magnet is rotated above a soft iron ring having a diameter of approximately 600 mm. Soft iron is used because it helps to guide the magnetic flux and concentrate the magnetic field lines through the AMRs. However, iron is also a good conductor of electrical current, and this property brings about potential issues for applications with time-varying magnetic fields. In fact, it is well known that when moving a magnet past a conductor, the changing magnetic flux induces circulating loops of current in it, called eddy currents. These loops of currents form on a plane perpendicular to the fluctuating magnetic field axis. If present, the energy of the eddy currents creates a braking torque acting on the magnet itself, which is dissipated as heat in the iron ring. Lamination is a classical technique for reducing eddy currents, which has been reported for other AMR devices (Lozano et al., 2016) and was also implemented on the iron ring in this design.

In the original version of the magnetocaloric heat pump, the iron teeth were laminated, but the iron ring was solid. In the earlier stages of the machine design it was assumed that the effect would be worst in the iron teeth, and that lamination of the ring was not needed. However, earlier testing of the original MagQueen revealed a weakness in the design related to the eddy currents inside the solid part of the iron ring, formed during the operation of the device. This aspect became more prominent as negatively affecting the performance, especially when the permanent magnet was rotated at higher frequencies. Therefore, as a result of the generation of the eddy currents, severe effects on the machine operational characteristics were observed: an increase of the required input work to the motor, heating of the iron ring and a braking torque acting on the magnet, proportional to its rotational frequency. These factors drastically limited the ability of MagQueen to run at higher frequencies. Therefore, we laminated not only the teeth but the entire iron ring (Figure 5a and Figure 5b). Eddy currents in the soft iron yoke depend on the cross-sectional area of the yoke material, specifically, the cross-section in the radial direction. The requirements for lamination were studied numerically, and, consequently, it was decided to build up the new ring from 4 mm thick plates laminated by epoxy in the radial direction with respect to the magnet axis.

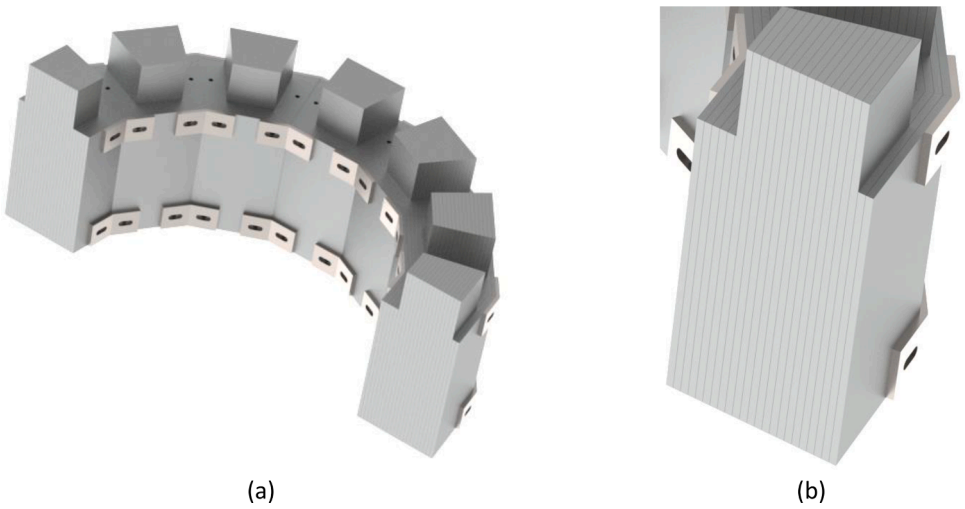

Fig. 5. (a) 3D cross section view of the laminated ring and (b) close-up view of the laminations.

2.3. AMR geometry

The core elements of the prototype are the beds containing the magnetocaloric material, i.e., the regenerator beds. They are all independent of each other and can be installed, removed and analysed individually. The housing of the regenerator bed is 3D printed in nylon using the Selective Laser Sintering (SLS) technique, which yielded a functional nylon regenerator housing with good mechanical properties. The choice of the housing material is important, since for housing materials with sufficient thermal diffusivity, axial conduction in the wall can affect the regenerator performance and apparent heat transfer coefficient (Nielsen et al., 2013), decreasing both the temperature span and the heating capacity.

Looking at Figure 6, it is immediately evident that the shape of the beds has a taper in the flow direction. The reason for this choice is explained and demonstrated in (Dall'Olio et al., 2017b), and in this work, we will only summarize the main advantages of tapering. First of all, tapering in the right direction does not have any evident disadvantages for AMR performance. Moreover, a negative tapering angle of around -10° gives a slight performance improvement with respect to the 0° channel. The reason is due to the key role that viscosity plays inside the regenerator. By having a wider flow channel at the cold end, the viscous losses are reduced because the flow area is larger compared to the regenerator hot side. Additionally, the improvement of the performance increases with frequency. Considering the geometrical point of view, in the radial distribution of regenerators, tapering gives a significant space optimization advantage compared to the parallel wall configuration. The empty bed volume is about 64.22 cm^3. Each of the 13 regenerator beds contains around 262 g of MCM, occupying a volume of 60.29 cm^3, having a porosity of around 0.38. The internal height of the housing is 17 mm, and the tapering angle is 10°. The flow resistance of the packed bed and the design of the screen supports ensure an even flow distribution, despite the tapering. Each bed has two inlet and two outlet ports to avoid dead volume losses, and the lid is made of non-magnetic stainless steel.

In the design of the regenerator, particular attention has been paid to the flow distribution inside the bed and the reduction of the heat transfer from the casing to the ambient. In this process, we conducted a thorough optimization of the housing by performing a number of simulations, both of the flow inside the bed and of the thermal losses through the housing walls. The main results of this study are a reduction of the dead volume at the inlet and the outlet of the regenerator, and a drastic drop of the heat transfer losses from the bottom surface of the regenerator. This goal was achieved with a specific embossment of the surface directly in contact with the iron tooth, together with the installation of an insulator between the lid and the MCM. Specifically, minimizing the dead volumes of the regenerator through optimization, we were able to exploit this undesirable volume as a very compact flow distributor, allowing the heat transfer fluid to be distributed evenly into the MCM. From a mechanical point of view, the average thickness of the

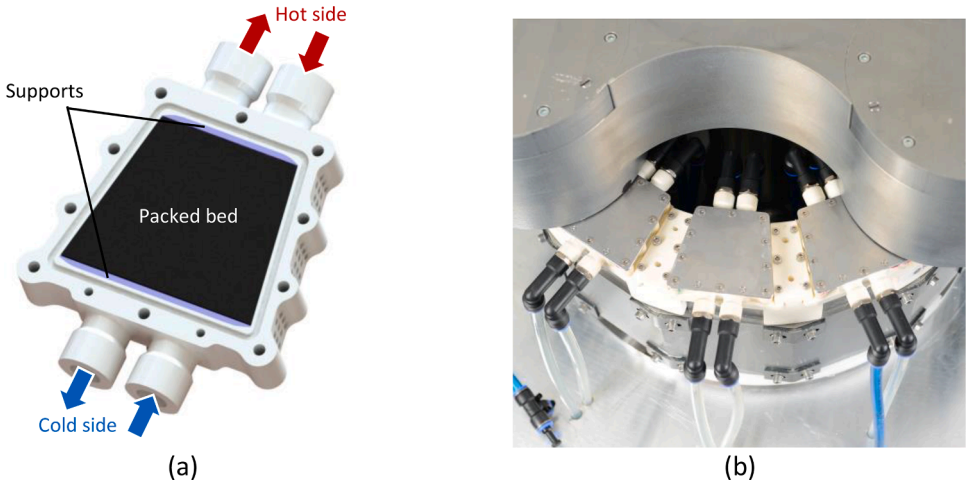

Fig. 6. (a) CAD model of the tapered bed and (b) photo of the beds installed on MagQueen.

regenerator housings has been calculated to have a maximum local wall deformation of 0.3 mm under a pressure of 1.5 bar and to resist a fluid pressure up to 5 bar (Dall'Olio et al., 2017a).

2.4. Regenerator materials

Once the regenerator housing geometry has been fixed, the next step is the filling of the regenerator with MCM. This represents what we could call the 'filling strategy' of the regenerator. The main steps of this process could be identified as the following: choose the MCM, fix the number of layers, decide the T_{Curie} and, finally, choose the single material percentage over the entire volume available inside the regenerator. Considering the material in MagQueen we chose La(Fe,Mn,Si)$_{13}$H$_y$, produced by Vacuumschmelze GmbH & Co. KG in Germany under the tradename CALORIVAC HS (Barcza et al., 2011), because it can be alloyed to give Curie temperatures throughout the design operating range of MagQueen. It is available as spherical particles, has attractive magnetocaloric properties, and should be mechanically robust.

Once the MCM family was chosen, the number of layers was fixed to 10. This amount is a balance between maximizing the magnetocaloric effect in the regenerator with practical issues related to material production and the process of filling the regenerator. The total length available for the MCM is 59 mm and having too short layers can result in high uncertainty during the filling process of the regenerator. Regarding the Curie temperature distribution, it is strongly related to the design hot and cold side temperatures. The design temperature span has been fixed to 20 K, covering the range from 1°C to 21°C with a uniform Curie temperature spacing of ΔT= 2.2 K. These nominal, or desired, T_{Curie} values are given in Table 2, along with the nominal composition. Uniform spacing between the layers had been specified. However, there is a material production tolerance in precise tuning of the T_{Curie}. Hence, the variation in the T_{Curie} can be considered as one of the factors hampering the best AMR performance (Lei et al., 2016a). The volume fraction of each T_{Curie} layer was then optimized using a 1D model as described in (Lei et al., 2015), and for our purpose, it was adapted to simulate tapered bed regenerators with a specific layering of MCM along the regenerators.

Based on AMR modelling results, including the tapered shape of the regenerator, we decided to use a constant magnetic energy approach to fix the fraction of each MCM material. After calculating the applied field, a geometrical approach was used to directly compute the subdivision into layers such that the total magnetic energy of each layer was equal. For each layer, the magnetic energy is found by the integral,

$$E_{mag} = \int_0^L \| B\|^2 dV \tag{2}$$

Since the total number of MCM layers was fixed to 10, we imposed that the volume of each MCM would have the same amount of magnetic energy to find the individual values of L. As a result, we obtained the fraction and consequently the length of each MCM layer, as shown in Figure 7. Unpublished modelling results showed that layering the regenerator in such a way to achieve constant magnetic energy per layer over the length of the AMR (compared to, e.g., constant length per layer, constant volume per layer, or constant magnetic flux per layer) was the best strategy to achieve the highest cooling performance.

Table 2
Nominal compositions of the ten materials and the distribution of Curie temperatures along the regenerator bed. All compositions are hydrated to saturation, so y is always approximately 1.65. The target T_{Curie} distribution is the ordered values and the received materials are given as actual T_{Curie}.

Layer	Nominal composition	Target T_{Curie} [K]	Actual T_{Curie} [K]
1 (hot side)	$LaFe_{11.19}Mn_{0.44}Si_{1.37}H_y$	294.2	292.1
2	$LaFe_{11.18}Mn_{0.45}Si_{1.37}H_y$	291.9	290.1
3	$LaFe_{11.17}Mn_{0.47}Si_{1.37}H_y$	289.7	288.7
4	$LaFe_{11.15}Mn_{0.48}Si_{1.37}H_y$	287.5	287.0
5	$LaFe_{11.14}Mn_{0.49}Si_{1.37}H_y$	285.3	283.8
6	$LaFe_{11.12}Mn_{0.51}Si_{1.37}H_y$	283.1	282.6
7	$LaFe_{11.11}Mn_{0.52}Si_{1.37}H_y$	280.8	280.6
8	$LaFe_{11.10}Mn_{0.53}Si_{1.37}H_y$	278.6	278.4
9	$LaFe_{11.09}Mn_{0.55}Si_{1.37}H_y$	276.4	275.8
10 (cold side)	$LaFe_{11.07}Mn_{0.56}Si_{1.37}H_y$	274.2	273.1

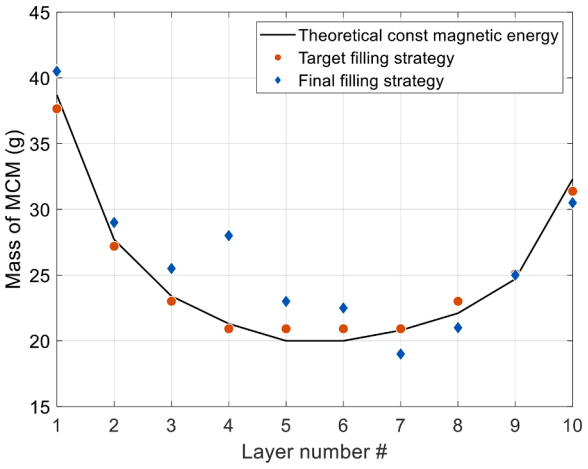

Fig. 7. Regenerator filling strategy showing the target and final filling strategy based on the material masses delivered by Vacuumschmelze GmbH & Co. KG.

Based on our simulation results, the MCM was ordered in mass quantities corresponding to the target filling strategy and for the nominal Curie temperature distribution. Spherical CALORIVAC HS was chosen for the MCM, because the spherical particles were shown to have a better heat transfer to pressure drop ratio compared to irregular particles of the same material family (Lei et al., 2018). The regenerators were built from loose particles without epoxy. The particle size was specified as the smallest producible size, which are particles with diameters in the range of 0.4-0.63 mm. Figure 7 shows the mass of MCM per layer according to the target (ideal) filling strategy. However, producing CALORIVAC-HS is still at an experimental stage, so the amounts of MCM supplied by the producer varied from the ordered amounts.

The regenerators were filled while mounted with the axis of the flow ports pointed vertically. A separating screen mesh was glued to a support, and the support was glued to the bottom (hot side) of the regenerator housing before filling (see Figure 6a). The materials were added one at a time, and each layer was compacted before the next material was added. A flat spoon was designed ad-hoc to fit into the regenerator, compress the material, and accomplish a uniform packing. Figure 8 shows one regenerator after filling. Once all ten layers were added, another screen mesh with a support was installed at the top (cold side) and glued to the housing. The inset in Figure 8 shows a light microscope image of neighboring particles of layer #4 and #5. Clearly, the La(Fe,Mn,Si)$_{13}$H$_z$ comes in different smooth shapes and sizes due to the manufacturing process of the MCM. For instance, particles in layer #4 are very homogeneous and have mostly spherical shapes, while particles in layer #5 have more rod-like shapes. In total, 3.41 kg of MCM was used in MagQueen. A silicon foam sheet is placed on top of the regenerator bed and under the metal lid both to hold the MCM under constant compression and flow channelling. By compressing the particle bed, migration of particles and formation of void regions can be prevented. The total dead volume can then be estimated from the two plastic supports that were glued into the housing at both ends of the particle bed. There is a total of 2.38 cm^3 of non-magnetic material at the cold end and 1.55 cm^3 at the hot end. Of that, 1.15 cm^3 at the cold end and 0.72 cm^3 at the hot end is dead volume occupied by fluid, equivalent to about 3% of the total volume.

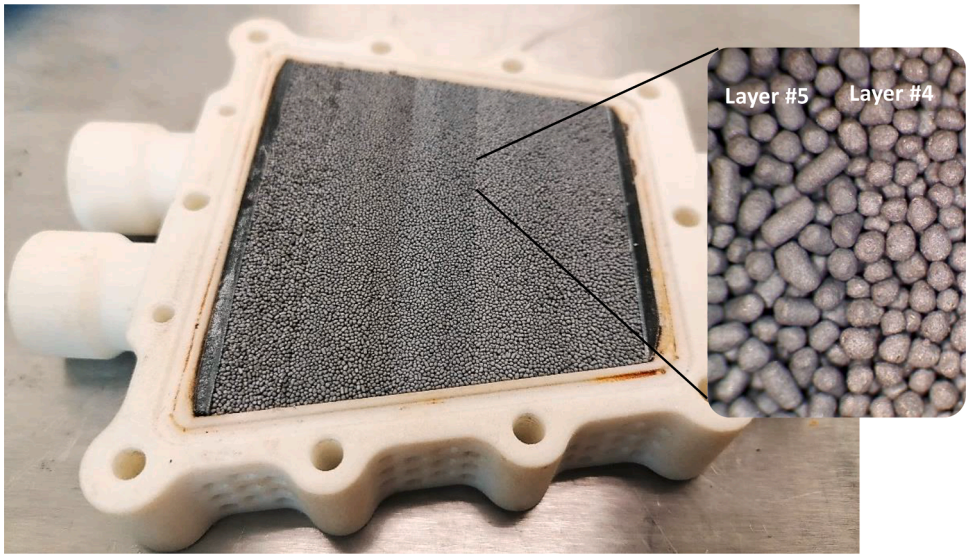

Fig. 8. AMR bed after manual filling and a microscopy image of particles at the intersection between two layers of the MCM.

2.5. Flow circuit and control

The main characteristics that a flow system should guarantee to achieve the optimum performance of an AMR can be summarized as the following:

1 Possibility to adjust the opening/closure timing of the valves according to the magnetization/demagnetization of each bed, both in the hot and cold blow
2 High temporal accuracy in synchronization with the magnet
3 Fast response of the active components, i.e. the valves, of around 1 ms
4 Low electrical power consumption of the components
5 Same inlet pressure for every channel
6 Low pressure losses
7 During the blows, same flow rate in each channel
8 Easy to access system

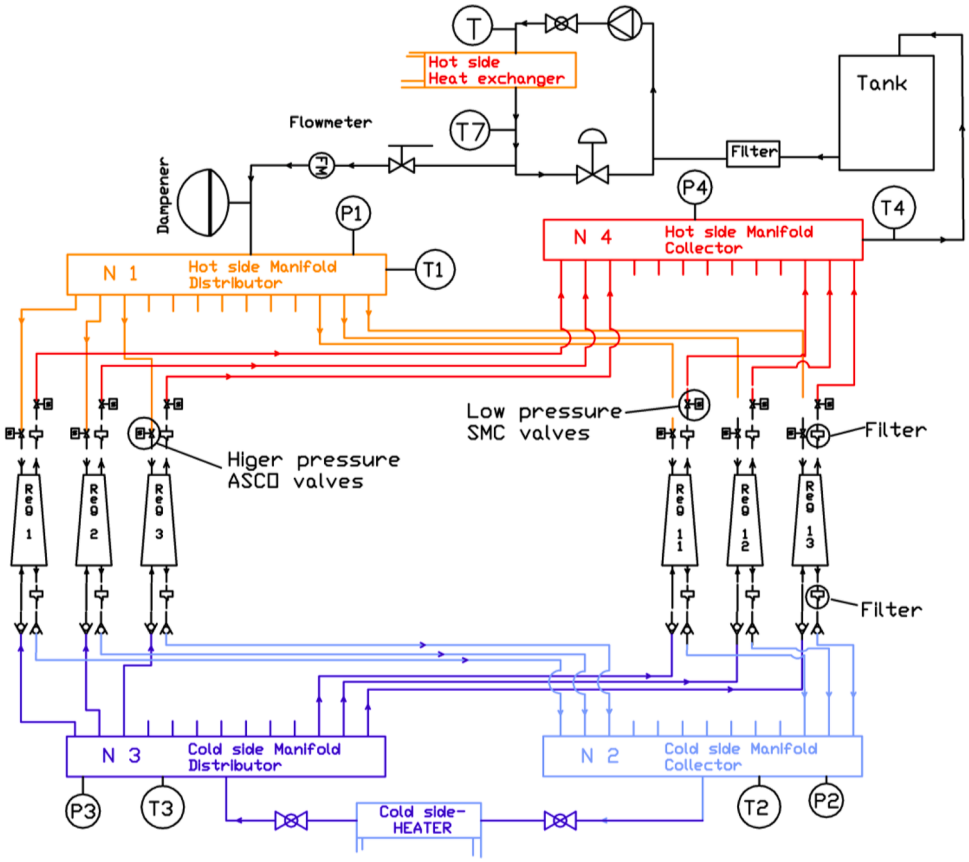

Fig. 9. Simplified schematic of the flow system for MagQueen.

Therefore, we designed and built our flow system in a way to satisfy all these prerequisites, and a simplified scheme of the flow system is reported in Figure 9. The heat transfer fluid is a mixture of water and 2% of ENTEK FNE (MacDermid Enthone GmbH, Germany), an additive that avoids MCM corrosion and consequent degradation. The complete flow system in MagQueen consists of 26 solenoid valves (2 for each bed), a pump, 26 check valves (two for each bed) and four manifolds (hot inlet, hot outlet, cold inlet, and cold outlet), two heat exchangers and a pressure damper. Additionally, filters were installed to protect the flow control valves. Piloted solenoid valves are connected to the hot inlet manifold because that set of valves experiences the highest pressure (at the pump outlet) and the piloted valves can seal over a higher-pressure differential. At the hot outlet manifold, the maximum pressure is low enough for a direct-acting solenoid valve. The passive check valves are mounted at the cold side of each regenerator. The pump operates continuously, meaning that the same volume of heat transfer fluid must always flow to the hot side inlet (connected to the pump outlet) as from the hot side outlet (connected to the pump suction side). The bridge between the position of the magnet and the electronics governing the valves is the absolute encoder mounted on the main shaft. This component constantly acquires the instantaneous angular position of the magnet. Since the inlets of all 13 regenerator beds are hydraulically coupled in parallel, the flow can be distributed in any desired manner according to the timing of the valves connected to the regenerator beds. There are safety mechanisms such as pressure relief valves installed in the device to protect the pump and avoid over-pressurization if there are no open flow paths through the regenerators. The magnet has two poles, which means that there are two sets of regenerators experiencing a high field at any given time, two sets of regenerators experiencing a low magnetic field, and two sets of regenerators on either side of each pole that experience some intermediate magnetic field.

Flow to each regenerator bed is controlled by the solenoid valves mounted on the hot side of the regenerator. Check valves on the cold side ensure that the flow from the hot side inlet is guided to the cold side outlet manifold, and the flow through the hot side outlet manifold travels from the cold side inlet manifold. Solenoid valve operation is position-controlled, meaning that a valve control algorithm implemented in LabVIEW monitors the position of the spinning magnet using the encoder reading and opens and closes the solenoids at the appropriate time. The open and closing angle of each solenoid is read from a table, allowing the operator to individually control the hot-to-cold and cold-to-hot fluid flow to each regenerator bed. The values can be changed while the device is in operation allowing for adjustment on-the-fly. This level of control allows for testing the sensitivity to length of the fluid flow period, timing of the flow period relative to the magnetic field, and testing how the regenerator beds interact with each other hydraulically. All these components, working harmoniously together allow for continuous and unidirectional flow through the system, while ensuring a reciprocating flow in each individual regenerator bed. The hot and cold heat exchangers represent the hot and cold reservoirs of the system. In detail, the heating power ($\dot{Q}_h$) is rejected into the hot heat exchanger, which can keep a fixed hot reservoir temperature T_{hot}. This temperature is controlled by a chiller, while the cooling load ($\dot{Q}_c$) is given by an electronically controlled heater installed in the cold reservoir heat exchanger. The temperature is measured across every single component of the system, while pressure is measured in the three higher pressure manifolds.

2.6. MagQueen live operation

Videos of the MagQueen operation are shown in Multimedia Component 1 and Multimedia Component 2. If we look at its operational characteristics, the first input is given to the motor that rotates the magnet, with a rotational frequency that can go up to 3 Hz AMR frequency with the current drive. The electronic control strategy is written in LabVIEW. It acquires the position of the magnet instantaneously via the encoder while opening and closing the valves for each bed according to the single valve operating interval. These windows can be modified on the fly, giving a unique and powerful tool to vary the working condition of the regenerators, which allows observing immediately the impact on the machine performance. The same principle is also valid for T_{hot} and the flow rate. The chiller and the heat exchangers allow to keep a constant temperature at the hot side of the regenerators, and the pump can change very quickly its velocity and therefore the flow rate.

3. Performance metrics

The performance of the MagQueen prototype was evaluated by the COP and the second-law efficiency. Since it provides both heating and cooling, the COP of the heat pump depends on its operation mode. In general, the heating load supplied to the hot sink ($\dot{Q}_h$) equals the heat removed from the cold source ($\dot{Q}_c$) plus the input power to the cycle. Hence, the heating COP (COP_h) is always 1 greater than the cooling COP (COP_c). The heating COP can then be defined as follows:

$$COP_h = \frac{\dot{Q}_h}{\dot{W}_{pump} + \dot{W}_{mag}} \tag{3}$$

Where $\dot{W}_{pump}$ corresponds to the pumping power needed to move the fluid, and $\dot{W}_{mag}$ is the magnetic (or AMR) power into the regenerator. It should be noted that the COP reported here is based on the shaft power input and does not include the efficiency of the drive system or the pump. The hydraulic pumping power is calculated as the product of fluid flow rate and the pressure drop through the AMR system, and it is given by:

$$\dot{W}_{pump} = \dot{V}(p_1 - p_2 + p_3 - p_4) \tag{4}$$

Where $\dot{V}$ is the volume flow rate, and p_1, p_2, and p_3 are the pressures measured in the three manifolds (see Figure 9). The employed pump is not optimized for the specific operating points, and thus an efficiency of 1 is assumed. For a product application where the pump can be designed specifically for the intended use, the efficiency of this should be included. The pressure p_4 is atmospheric pressure and is thus 0. This equation ensures that the pumping power is not a function of the specific heat exchanger chosen. Here the pressures p_2 and p_3 are quite similar, as the cold heat exchanger is actually a large electric heater.

The measured shaft power ($\dot{W}_{shaft}$) required to rotate the magnet assembly is defined as:

$$\dot{W}_{shaft} = 2\pi f \Gamma \tag{5}$$

Where f is the operating frequency (equal to that of the motor frequency), which is half of the AMR frequency, as two high field and two low field regions are produced for one rotation of the permanent magnet (see Figure 4). Γ is the shaft torque.

Subtracting the power losses ($\dot{W}_{losses}$) associated with both eddy currents induced in the laminated iron ring and friction in the bearings gives $\dot{W}_{mag}$ as:

$$\dot{W}_{mag} = \dot{W}_{shaft} - \dot{W}_{losses} \tag{6}$$

The supplied heat ($\dot{Q}_h$) is estimated to equal the corresponding amount of cooling load ($\dot{Q}_c$) plus the work input by the AMR ($\dot{W}_{pump} + \dot{W}_{mag}$):

$$\dot{Q}_h = \dot{Q}_c + \dot{W}_{mag} + \dot{W}_{pump} \tag{5}$$

Where $\dot{Q}_c$ is calculated based on:

$$\dot{Q}_c = \dot{V}\rho_f c_f \Delta T_{cold} \tag{6}$$

Where c_f is the specific heat capacity of water, ρ_f is the density of water, and ΔT_{cold} is the temperature difference of the fluid between the

in-and outlet of the cold side, i.e., T_3-T_2.

The second-law efficiency, η_{II}, is commonly used to compare different cooling systems. Here the cooling COP is as the baseline because it gives a better thermodynamic assessment of the system. It is a measure of the actual cooling performance relative to the performance under reversible conditions (i.e., the Carnot cooling cycle) and is given by:

$$\eta_{II} = \frac{\mathrm{COP}_c}{\mathrm{COP}_{ideal}} \tag{7}$$

Where COP_c is the cooling COP of the heat pump, and it is given by:

$$\mathrm{COP}_c = \frac{\dot{Q}_c}{\dot{W}_{pump} + \dot{W}_{mag}} \tag{8}$$

COP_{ideal} is the ideal or reversible Carnot COP for a cooling cycle, i.e., the maximum performance that can be obtained by the heat pump. In terms of hot and cold reservoir temperatures, it can be expressed as:

$$\mathrm{COP}_{ideal} = \frac{T_{cold}}{T_{hot} - T_{cold}} \tag{9}$$

The difference between the hot and cold reservoir temperature of the system is also referred to as the temperature span (ΔT_{span}) of the system. T_{hot} is assumed equal to T_1 that is temperature of the fluid entering the AMRs from the hot side during the cold blow, while T_{cold} is equal to T_3, which is the temperature entering the regenerators from the cold side during the hot blow (see Figure 9). The heating COP can then be calculated from the second law efficiency:

$$\mathrm{COP}_h = \eta_{II}\frac{T_{cold}}{T_{hot} - T_{cold}} + 1 \tag{10}$$

4. Results and discussion

In the first set of experiments, the influence of the cold reservoir temperature on the device performance was investigated by varying the cooling load simulated by the circulation heater, i.e., the cold reservoir temperature. As expected for first-order phase transition materials performance is very sensitive to the hot reservoir temperature (Lei et al., 2016a). Initial tests found that 295 K was the optimum, so this was kept constant in the following. The experimental results presented in Figure 10a and Figure 10b were obtained when operating the device at a constant cycle frequency of 0.5 Hz, and a volumetric flow rate of 500 L/h. The average blow fraction, which was defined as the time fraction of the AMR cycle when fluid is blown through the regenerator (Fortkamp et al., 2018; Nakashima et al., 2017), was fixed at 36 % in the cold-to-hot and hot-to-cold directions.

Studies have shown that the magnetocaloric effect represented as the isothermal entropy change or adiabatic temperature change in FOPT materials occurs over a narrow temperature range and that the MCE rises to higher temperatures with increasing magnetic field (Lei et al., 2016a; Vieira et al., 2021). For this reason, the hot reservoir (working) temperature was fixed at 295 K, which is higher than the hottest Curie temperature of 292 K of the multi-layer AMR beds. It can be observed that the heating power and device efficiency decrease, as the temperature span increases (i.e., the cold reservoir temperature decreases). The trend resembles those reported in the literature (Huang et al., 2019; Jacobs et al., 2013). The MagQueen prototype provided a peak heating power of 340 W with a heating COP of 6.7 while holding a temperature span of 10.3 K. Under these conditions, a maximum second-law efficiency of 20.6 % was obtained, which was higher than the AMR prototype previously developed by DTU (Eriksen et al., 2016).

To further explore the performance of the prototype, the heating power was measured at an increased cycle frequency of 1.2 Hz for different cold reservoir temperatures, while keeping the hot reservoir temperature at 295 K. The experimental results are shown in Figure 11a and Figure 11b. The device can realize higher heating capacities at a higher cycle frequency. At a span of 5.6 K and a flow rate of 1280 l/h, the device produced a peak heating power of around 950 W with a COP of 7.04. It is worth mentioning that the η_{II} for this case was 11.6 %.

As the cycle frequency increases, the COP of the MagQueen prototype decreases. Although higher heating capacities are achieved at a higher frequency, at the same time, the power input to the AMR increases faster. As reported by Trevizoli et al. (2016), the increasing power input can mainly be attributed to the increase in the pumping power, as higher fluid flow rates result in a larger system pressure drop. The large weight of the magnet is one of the disadvantages of the device architecture and limits the operating frequency of the AMR. Thanks to the use of bearings, the rotational friction is reduced to its minimum, and inertia is very low because the machine usually works at a constant speed. In fact, the motor can provide a maximum operating frequency of up to 3 Hz, equivalent to 6 Hz AMR frequency.

After the detailed description of the AMR device and after presenting some experimental tests, the pros and cons of the design can be discussed. One of the advantages of the rotating magnet design is the absence of rotary valves or rotary connections, which would increase the motor power due to friction and would probably cause leakage of the working fluid, over time. Another advantage is the presence of only a few constraints for the magnet design, whose volume can be extended in all directions to achieve the desired magnetic field in the air gap. Furthermore, due to the iron yoke design, the access and the installation of the regenerators is safe and easy with no need to remove heavy parts from the machine, like the magnet. Also, the inside of the regenerators can be examined easily by just untightening the screws that hold the lid in place.

Some of the design challenges are the quite complex flow system and the electronics controlling the MagQueen operation. The electrical power needed to operate the solenoid valves is kept low (of the order of 60 W in total) thanks to the use of low power consuming equipment, but

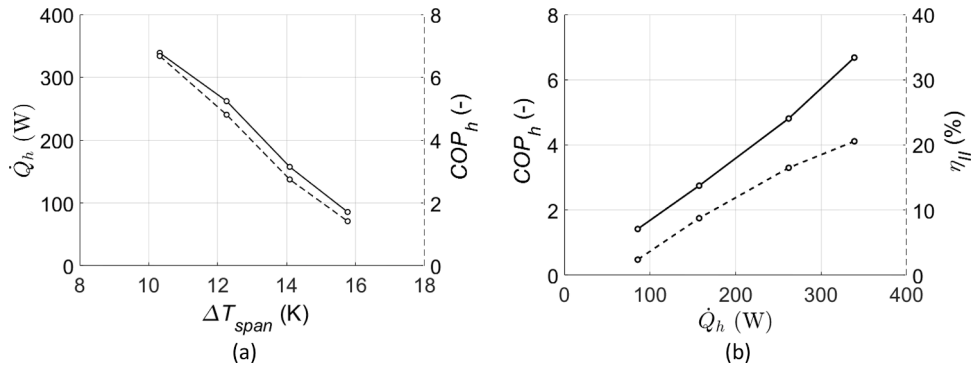

Fig. 10. (a) Heating power vs. temperature span for a hot reservoir temperature of 295 K.
(b) Heating performance map (heating COP vs. heating power) for a hot reservoir temperature of 295 K.

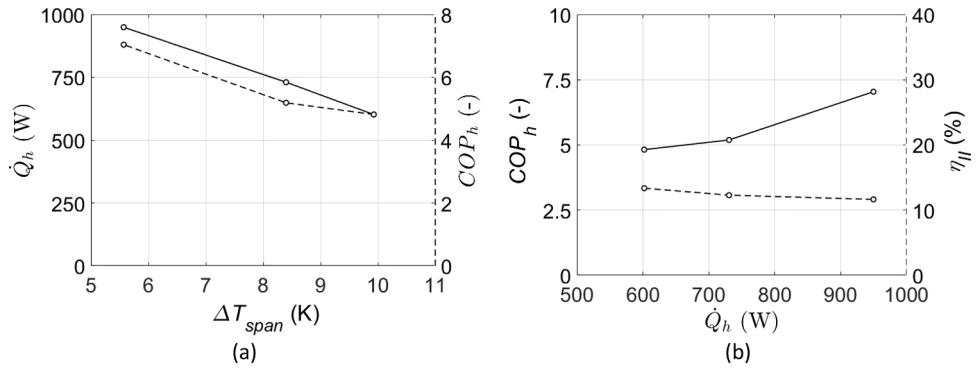

Fig. 11. (a) Heating power vs. temperature span at a frequency of 1.2 Hz. (b) Heating performance map (heating COP vs. heating power) for a hot reservoir temperature of 295 K.

this could be further reduced in a more compact design. As the yoke is a large iron mass and the regenerators are directly in contact with it, there is a heat leakage from the regenerators to the yoke. We tried to reduce this heat flow by reducing the contact surface between the yoke and the regenerators, and we were able to reduce the heat losses by up to 80 %. Concluding this analysis, we can say that our prototype can still be improved, for example in the compactness and total mass of the system, but the overall advantages of this design are sensible with respect to many other existing prototypes.

5. Conclusion

The detailed design of a novel magnetocaloric heat pump developed at DTU has been presented and discussed in detail. In this process, a deep scientific commitment to optimizing the components of the machine has been the main part of the work, resulting in a prototype with great potential regarding high efficiency and power. The experimental results showed that the prototype is capable of providing a heating power of 950 W while holding a temperature span of 5.6 K and at 1.2 Hz. The maximum second-law efficiency of 20.6 % was obtained when the device delivered a heating power of 340 W over a 10.3 K temperature span. The heating COP ranged between 6.7 and 1.4 for temperature spans between 10.3 and 15.7 at a cycle frequency of 0.5 Hz, while a maximum heating COP of 7.0 was found over a temperature span of 5.6 K when operating at 1.2 Hz. The versatility and robustness of the magnetocaloric heat pump allow for easy change of the regenerators, with the possibility to modify all flow parameters instantaneously and for each regenerator separately.

CRediT authorship contribution statement

S. Dall'Olio: Conceptualization, Methodology, Software, Validation, Writing – original draft, Writing – review & editing, Visualization. **M. Masche:** Conceptualization, Methodology, Software, Validation, Writing – original draft, Writing – review & editing, Visualization. **J. Liang:** Conceptualization, Methodology, Software, Validation, Writing – review & editing, Visualization. **A.R. Insinga:** Software, Investigation, Writing – review & editing, Visualization. **D. Eriksen:** Conceptualization, Methodology, Software, Validation, Writing – review & editing. **R. Bjørk:** Methodology, Validation, Writing – review & editing. **K.K. Nielsen:** Methodology, Software, Validation, Writing – review & editing. **A. Barcza:** Resources, Writing – review & editing. **H.A. Vieyra:** Resources, Writing – review & editing. **Niels V. Beek:** Resources, Writing – review & editing. **H. Neves Bez:** Investigation, Writing – review & editing. **K. Engelbrecht:** Conceptualization, Methodology, Validation, Writing – review & editing, Visualization, Funding acquisition. **C.R.H. Bahl:** Conceptualization, Methodology, Validation, Writing – review & editing, Visualization, Funding acquisition.

Declaration of Competing Interest

The authors declare that they have no known competing financial interests or personal relationships that could have appeared to influence the work reported in this paper.

Acknowledgements

This work was in part financed by the RES4Build project, which received funding from the European Union's Horizon 2020 research and innovation program under grant agreement No.814865 and the ENOVHEAT project which was funded by the Innovation Fund Denmark (contract no 12-132673). We wish to thank Mike Wichmann and Jørgen Geyti for their technical assistance in the construction of the MagQueen device. The authors also acknowledge Jens F. S. Borchsenius for electronic expertise. Tian Lei is acknowledged for his modeling work. Furthermore, the authors would like to thank Danish Decommissioning for helping with the exchange of the old solid iron ring.

Supplementary materials

Supplementary material associated with this article can be found, in the online version, at doi:10.1016/j.ijrefrig.2021.09.007.

References

Aprea, C., Greco, A., Maiorino, A., Masselli, C., 2016. The energy performances of a rotary permanent magnet magnetic refrigerator. Int. J. Refrig. 61, 1–11. https://doi.org/10.1016/j.ijrefrig.2015.09.005 https://doi.org/.

Aprea, C., Greco, A., Maiorino, A., Mastrullo, R., Tura, A., 2014. Initial experimental results from a rotary permanent magnet magnetic refrigerator. Int. J. Refrig. 43, 111–122. https://doi.org/10.1016/j.ijrefrig.2014.03.014 https://doi.org/.

Arnold, D.S., Tura, A., Ruebsaat-Trott, A., Rowe, A., 2014. Design improvements of a permanent magnet active magnetic refrigerator. Int. J. Refrig. 37, 99–105. https://doi.org/10.1016/J.IJREFRIG.2013.09.024 https://doi.org/.

Bahl, C.R.H., Engelbrecht, K., Eriksen, D., Lozano, J.A., Bjørk, R., Geyti, J., Nielsen, K.K., Smith, A., Pryds, N., 2013. Development and experimental results from a 1 kW prototype AMR. Int. J. Refrig. 37, 78–83. https://doi.org/10.1016/j.ijrefrig.2013.09.001 https://doi.org/.

Bansal, P., Vineyard, E., Abdelaziz, O., 2012. Status of not-in-kind refrigeration technologies for household space conditioning, water heating and food refrigeration. Int. J. Sustain. Built Environ. https://doi.org/10.1016/j.ijsbe.2012.07.003 https://doi.org/.

Barcza, A., Katter, M., Zellmann, V., Russek, S., Jacobs, S., Zimm, C., 2011. Stability and Magnetocaloric Properties of Sintered La(Fe, Mn, Si)13Hz Alloys. IEEE Trans. Magn. 47, 3391–3394. https://doi.org/10.1109/TMAG.2011.2147774 https://doi.org/.

Bjørk, R., Bahl, C.R.H., Nielsen, K.K., 2016. The lifetime cost of a magnetic refrigerator. Int. J. Refrig. 63, 48–62. https://doi.org/10.1016/j.ijrefrig.2015.08.022 https://doi.org/.

Bjørk, R., Bahl, C.R.H., Smith, A., Pryds, N., 2010. Review and comparison of magnet designs for magnetic refrigeration. Int. J. Refrig. 33, 437–448. https://doi.org/10.1016/j.ijrefrig.2009.12.012 https://doi.org/.

Cheng, Z., Jiaohong, H., Hongwei, Y., Peiyu, J., Juan, C., Cuilan, L., Zhaojie, L., Yingde, Z., 2016. Design and research of the room temperature magnetic wine cabinet. Refrigeration Science and Technology 63–66. https://doi.org/10.18462/iir.thermag.2016.0090.

Dall'Olio, S., Eriksen, D., Engelbrecht, K., Insinga, A.R., Bahl, C.R.H., 2017a. Design, enhanced thermal and flow efficiency of a 2 kW active magnetic regenerator. 9th World Conference on Experimental Heat Transfer, Fluid Mechanics and Thermodynamics 1–10.

Dall'Olio, S., Lei, T., Engelbrecht, K., Bahl, C.R.H., 2017b. The effect of tapering on a magnetocaloric regenerator bed. Int. J. Refrig. 84, 300–308. https://doi.org/10.1016/J.IJREFRIG.2017.08.012 https://doi.org/.

Dincer, I., Kanoğlu, M., 2003. Refrigeration Systems and Applications, 2nd ed. Wiley.

Eriksen, D., Engelbrecht, K., Bahl, C.R.H., Bjørk, R., 2016. Exploring the efficiency potential for an active magnetic regenerator Exploring the efficiency potential for an active magnetic regenerator. Sci. Technol. Built Environ. 22, 527–533. https://doi.org/10.1080/23744731.2016.1173495 https://doi.org/.

Eriksen, D., Engelbrecht, K., Bahl, C.R.H., Bjørk, R., Nielsen, K.K., Insinga, A.R., Pryds, N., 2015. Design and experimental tests of a rotary active magnetic regenerator prototype. Int. J. Refrig. 58, 14–21. https://doi.org/10.1016/j.ijrefrig.2015.05.004 https://doi.org/.

European Commission, 2019. European Green Deal [WWW Document]. URL https://ec.europa.eu/info/sites/info/files/european-green-deal-communication_en.pdf (accessed 6.5.21).

Fortkamp, F.P., Eriksen, D., Engelbrecht, K., Bahl, C.R.H., Lozano, J.A., Barbosa Jr., J.R., 2018. Experimental investigation of different fluid flow profiles in a rotary multi-bed active magnetic regenerator device. Int. J. Refrig. 91, 46–54. https://doi.org/10.1016/j.ijrefrig.2018.04.019 https://doi.org/.

Greco, A., Aprea, C., Maiorino, A., Masselli, C., 2019. A review of the state of the art of solid-state caloric cooling processes at room-temperature before 2019. Int. J. Refrig. 106, 66–88. https://doi.org/10.1016/j.ijrefrig.2019.06.034 https://doi.org/.

Gschneidner Jr., K.A., Pecharsky, V.K., 2008. Thirty years of near room temperature magnetic cooling: Where we are today and future prospects. Int. J. Refrig. 31, 945–961. https://doi.org/10.1016/j.ijrefrig.2008.01.004 https://doi.org/.

Huang, B., Lai, J.W., Zeng, D.C., Zheng, Z.G., Harrison, B., Oort, A., van Dijk, N.H., Brück, E., 2019. Development of an experimental rotary magnetic refrigerator prototype. Int. J. Refrig. 104, 42–50. https://doi.org/10.1016/j.ijrefrig.2019.04.029 https://doi.org/.

Insinga, A.R., Bjørk, R., Smith, A., Bahl, C.R.H., 2016. Globally Optimal Segmentation of Permanent-Magnet Systems. Phys. Rev. Appl. 5, 1–16. https://doi.org/10.1103/PhysRevApplied.5.064014 https://doi.org/.

Insinga, A.R., Smith, A., Bahl, C.R.H., Nielsen, K.K., Bjørk, R., 2019. Optimal Segmentation of Three-Dimensional Permanent-Magnet Assemblies. Phys. Rev. Appl. 12, 064034 https://doi.org/10.1103/PhysRevApplied.12.064034 https://doi.org/.

Jacobs, S., Auringer, J., Boeder, A., Chell, J., Komorowski, L., Leonard, J., Russek, S., Zimm, C., 2013. The performance of a large-scale rotary magnetic refrigerator. Int. J. Refrig. 37, 84–91. https://doi.org/10.1016/j.ijrefrig.2013.09.025 https://doi.org/.

Kitanovski, A., Tušek, J., Tomc, U., Plaznik, U., Ožbolt, M., Poredoš, A., 2015. Magnetocaloric Energy Conversion : From Theory to Applications. Springer.

Lei, T., Engelbrecht, K., Nielsen, K.K., Neves Bez, H., Bahl, C.R.H., 2016a. Study of multi-layer active magnetic regenerators using magnetocaloric materials with first and second order phase transition. J. Phys. D. Appl. Phys. 49 https://doi.org/10.1088/0022-3727/49/34/345001 https://doi.org/.

Lei, T., Engelbrecht, K., Nielsen, K.K., Neves, H., 2016b. Optimization of multi-layer active magnetic regenerator towards compact and efficient refrigeration. 29th Int. Conf. Effic. Cost, Optimisation, Simul. Environ. Impact Energy Syst 1–12.

Lei, T., Navickaitė, K., Engelbrecht, K., Barcza, A., Vieyra, H., Nielsen, K.K., Bahl, C.R.H., 2018. Passive characterization and active testing of epoxy bonded regenerators for room temperature magnetic refrigeration. Appl. Therm. Eng. 128, 10–19. https://doi.org/10.1016/j.applthermaleng.2017.08.152 https://doi.org/.

Lei, T., Nielsen, K.K., Engelbrecht, K., Bahl, C.R.H., Neves Bez, H., Veje, C.T., 2015. Sensitivity study of multi-layer active magnetic regenerators using first order magnetocaloric material La(Fe,Mn,Si)13Hy. J. Appl. Phys. 118, 014903 https://doi.org/10.1063/1.4923356 https://doi.org/.

Lionte, S., Barcza, A., Hittinger, M., Risser, M., Muller, C., Katter, M., 2018. Recent experimental results of first order LaFeSi-based magnetocaloric materials in an Active Magnetic Regeneration device. Refrigeration Science and Technology 56–61. https://doi.org/10.18462/iir.thermag.2018.0008 https://doi.org/.

Lozano, J.A., Capovilla, M.S., Trevizoli, P.V., Engelbrecht, K., Bahl, C.R.H., Barbosa Jr., J.R., 2016. Development of a novel rotary magnetic refrigerator. Int. J. Refrig. 68, 187–197. https://doi.org/10.1016/j.ijrefrig.2016.04.005 https://doi.org/.

Lozano, J.A., Engelbrecht, K., Bahl, C.R.H., Nielsen, K.K., Eriksen, D., Olsen, U.L., Barbosa Jr., J.R., Smith, A., Prata, A.T., Pryds, N., 2013. Performance analysis of a rotary active magnetic refrigerator. Appl. Energy 111, 669–680. https://doi.org/10.1016/j.apenergy.2013.05.039 https://doi.org/.

Monfared, B., Palm, B., 2016. New magnetic refrigeration prototype with application in household and professional refrigerators. Refrigeration Science and Technology 146–149. https://doi.org/10.18462/iir.thermag.2016.0142 https://doi.org/.

Nakashima, A.T.D., Dutra, S.L., Barbosa Jr., J.R., 2017. Experimental Evaluation of the Flow Imbalance in an Active Magnetic Experimental. 9th World Conf. Exp. Heat Transf. Fluid Mech. Thermodyn.

Nielsen, K.K., Nellis, G.F., Klein, S.A., 2013. Numerical modeling of the impact of regenerator housing on the determination of Nusselt numbers. Int. J. Heat Mass Transf. 65, 552–560. https://doi.org/10.1016/j.ijheatmasstransfer.2013.06.032 https://doi.org/.

Okamura, T., Hirano, N., 2013. Improvement of the performance of a room temperature magnetic refrigerator using Gd-alloy. J. Japan Soc. Appl. Electromagn. Mech. 21, 10–14.

Qian, S., Nasuta, D., Rhoads, A., Wang, Y., Geng, Y., Hwang, Y., Radermacher, R., Takeuchi, I., 2016. Not-in-kind cooling technologies: A quantitative comparison of refrigerants and system performance. Int. J. Refrig. 62, 177–192. https://doi.org/10.1016/J.IJREFRIG.2015.10.019 https://doi.org/.

RES4BUILD [WWW Document], 2021. URL https://res4build.eu/about/project-overview/ (accessed 8.8.21).

Rowe, A.M., Barclay, J.A., 2003. Design of an active magnetic regenerator test apparatus. Am. Inst. Phys. (AIP) 995–1002. https://doi.org/10.1063/1.1472121 https://doi.org/.

Sota, G., Kawanami, T., Yamashita, K., Onishi, T., Soejima, K., Wada, H., Hirano, S., Okamura, T., Bae, S., Hirano, N., Shirai, K., Hirasawa, S., 2016. Performance analysis of magnetocaloric heat pump with manganese-based compounds as a magnetic refrigerant. Ecos 2016 - Proceedings of the 29th International Conference on Efficiency. Cost, Optimisation, Simulation and Environmental Impact of Energy Systems.

Teyber, R., Trevizoli, P.V, Christiaanse, T.V, Govindappa, P., Niknia, I., Rowe, A., 2017. Permanent magnet design for magnetic heat pumps using total cost minimization. J. Magn. Magn. Mater. 442, 87–96. https://doi.org/10.1016/j.jmmm.2017.06.039 https://doi.org/.

Trevizoli, P.V., Lozano, J.A., Peixer, G.F., Barbosa Jr., J.R., 2015. Design of nested Halbach cylinder arrays for magnetic refrigeration applications. J. Magn. Magn. Mater. 395, 109–122. https://doi.org/10.1016/j.jmmm.2015.07.023 https://doi.org/.

Trevizoli, P.V, Nakashima, A.T., Peixer, G.F., Barbosa Jr., J.R., 2016. Performance evaluation of an active magnetic regenerator for cooling applications – part I : Experimental analysis and thermodynamic performance. Int. J. Refrig. 72, 192–205. https://doi.org/10.1016/j.ijrefrig.2016.07.009 https://doi.org/.

Tura, A., Rowe, A., 2010. Permanent magnet magnetic refrigerator design and experimental characterization. Int. J. Refrig. 34, 628–639. https://doi.org/10.1016/j.ijrefrig.2010.12.009 https://doi.org/.

Tušek, J., Zupan, S., Šarlah, A., Prebil, I., Poredos, A., 2010. Development of a rotary magnetic refrigerator. Int. J. Refrig. 33, 294–300. https://doi.org/10.1016/j.ijrefrig.2009.11.003 https://doi.org/.

Vieira, B.P., Bez, H.N., Kuepferling, M., Rosa, M.A., Schafer, D., Plá Cid, C.C., Vieyra, H. A., Basso, V., Lozano, J.A., Barbosa Jr., J.R., 2021. Magnetocaloric properties of spheroidal La(Fe,Mn,Si)13Hy granules and their performance in epoxy-bonded active magnetic regenerators. Appl. Therm. Eng. 183, 116185 https://doi.org/10.1016/j.applthermaleng.2020.116185 https://doi.org/.

Yu, B., Liu, M., Egolf, P.W., Kitanovski, A., 2010. A review of magnetic refrigerator and heat pump prototypes built before the year 2010. Int. J. Refrig. 33, 1029–1060. https://doi.org/10.1016/j.ijrefrig.2010.04.002 https://doi.org/.

J. A. Barclay, "A Review Of Magnetic Heat Pump Technology," Proceedings of the 25th Intersociety Energy Conversion Engineering Conference, 1990, pp. 222-227, doi: 10.1109/IECEC.1990.716573.